Version: June 30, 2017

PAIR DISTRIBUTION FUNCTION ANALYSIS APPLIED TO DECAHEDRAL GOLD NANOPARTICLES

H. Nakotte[1,*], C. Silkwood[1], K. Page[2,3], H.W. Wang[2,3], D. Olds[2,3], B. Kiefer[1], S. Manna[4], D. Karpov[1], E. Fohtung[1,3] and E. E. Fullerton[4]

[1]Department of Physics, New Mexico State University, Las Cruces, NM 88003, USA
[2]Spallation Neutron Source, Oak Ridge National Laboratory, Oak Ridge, TN 37830, USA
[3]Los Alamos Neutron Science Center, Los Alamos National Laboratory, Los Alamos, NM 87545, USA
[4]Center for Memory and Recording Research, University of California – San Diego, La Jolla, CA 92093, USA

Abstract:

The five-fold symmetry *fcc*-derived nanoparticles is inconsistent with the translational symmetry of a Bravais lattice and generally explained by multiple twinning of a tetrahedral subunit about a (joint) symmetry axis, with or without structural modification to the *fcc* motif. Unlike bulk materials, five-fold twinning in cubic nanoparticles is common and strongly affects its structural, chemical and electronic properties. To test and verify theoretical approaches, it is therefore pertinent that the local structural features of such materials can be fully characterized. The small size of nanoparticles severely limits the application of traditional analysis technique, such as Bragg diffraction. A complete description of the atomic arrangement in nanoparticles therefore requires a departure from the concept of translational symmetry and do not allow fully evaluating all the structural features experimentally. We describe how recent advances in neutron and synchrotron sources and instrumentation, together with the increasing power of computing, are shaping the development of alternative analysis methods of scattering data for nanostructures. We present the application of Debye scattering and Pair Distribution Function (PDF) analysis towards modeling of the total scattering data for the example of decahedral gold nanoparticles. PDF measurements provide a statistical description of the pair correlations of atoms within a material, and it evaluates the probability of finding two atoms within a given distance of a material. We explored the sensitivity of existing neutron and synchrotron X-ray PDF instruments using three different simple models for our gold nanoparticles: a multiply-twinned *FCC* decahedron model, a relaxed body-centered orthorhombic (*bco*) and a hybrid model. The predictions of the three models were then compared with experimental data from synchrotron X-

rays and we present our experimentally derived atomistic models of the gold nanoparticles, with surprising results and a perspective on remaining challenges. Our findings provide evidence for the suitability of PDF analysis in the characterization of other nanosized particles that may have commercial applications.

Corresponding Author:

Heinz Nakotte
Department of Physics
MSC 3D
New Mexico State University
Las Cruces NM 88003, USA
Phone: *1-575-646-2459
E-mail: hnakotte@nmsu.edu

1. Introduction and Motivation

Due to their structural and functional diversity at the nanoscale, gold particles and rods have tremendous potential in a wide variety of emerging technologies, such as photovoltaics [1], nanoelectronics [2], and high-resolution spectroscopy [3], or targeted radiation treatments for cancer [4], biological imaging [5], and biosensors [6]. Gold nanocrystals are attracting increasing interest within the scientific community due to the inherent differences between their electronic properties compared to their bulk counterparts and their optical properties strongly depend on the size, morphology and strain. [7,8] Bulk' gold particles crystallize in the face-centered-cubic (*fcc*) structure with a lattice parameter of 4.07 Å at room temperature, and the nearest-neighbor gold distance is 2.87 Å. For gold nanoparticles, however, several highly geometric polyhedral shapes have been reported. Thus, the investigation of nanoscale internal structure, shape, and lattice strain is crucial for the rational design of suitable synthesis techniques and in understanding growth dynamics on the nanoscale. Among others, nanoscale structural features may alter the contributions due to dominant surface effects. As particle sizes approach atomic length scales, the discreteness of matter and the fluctuations in interatomic forces enhance many effects, which are absent or insignificant at larger length scales, thereby leading to 'quantum-confinement' effects that are absent in the atomic and bulk limits. The development and testing of reliable theoretical and computational models requires in-depth experimental verification of the local structure in nanoparticles. Novel nanostructure synthesis techniques have enabled more precise control over the sizes and shapes of metal nanoparticles, and some of us recently reported on the use thermal chemical vapor deposition (CVD) to design a variety of gold nanoparticle shapes. [9]

In this paper, we explore whether current state-of-the-art pair-distribution-function (PDF) analysis and instrumentation may provide insight into the local structure for the case of such CVD-grown decahedral gold nanoparticles, which have attracted much recent attention because of their five-fold symmetry. To date, observations of five-fold twinning have been made almost exclusively with electron microscopy. [10] Because of the scale of the particles, electron microscopy has been as the method of choice for characterizing nanoscale structures. The first diffraction image of a five-fold particle was produced using the technique selected area electron diffraction. In the beam of electrons directed at a sample, the wavelength of $\sim 10^{-12}\ m$. Electrons have a shorter de Broglie wavelength and consequently higher spatial resolving power. High-

resolution electron microscopy enabled the observation of the five subunits, but such studies have had limited success to distinguish between models predicting the strain states of such nanoparticles. [11] One of the greatest barriers to progress is the lack of experimentally derived atomistic models for such nanoparticles. Although structural characterization tools at nanoscale exist, in practice, it is very challenging to characterize them to the same level of detail as their bulk counterparts. The inherently accessible scale of any one measurement type limits the accuracy of overall model fidelity. Through a variety of scattering probe measurements combined with theory, we gain access to the detailed atomistic scale of such novel gold nanoparticles. The main purpose of this paper is to explore the prospects of Pair-Distribution-Function (PDF) Analysis as an alternative and complementary approach for resolving the local structure of nanoparticles.

2. Equilibrium Cluster Computations

The shape of clusters of atoms is determined by the competition of bulk *vs.* surface and strain energies. These competing energies may lead (and often do lead) to geometric polyhedral shapes that depend on particle size and sample environment. In 2005, Baletto and Ferrando published a review article discussing the energetics and stability ranges for different geometrical shapes for isolated nanoparticles grown at equilibrium conditions. [12] To corroborate their findings, we performed a small number of cluster computations for gold nanoparticles at equilibrium conditions using the GLUE potential, which was generated by fitting the potential to materials properties of elemental Au, including the its cohesive energy and (111) surface energy [13] All clusters were relaxed to their ground state energy at T = 0 K, neglecting zero-point-energy and any thermal energy contributions. All computations were performed using the software package GULP.). [14,15] We computed the relaxed energies for Mackay (icosahedral, Ih), Marks (decahedral, Dh), truncated octrahedal (TO), tetrahedral, hexagonal and spherical clusters for up to 3000 gold atoms. It should be noted, that the calculations will converge toward space-filling solutions.

Our calculations reveal that the spherical shape is less favorable for gold than some of the polyhedral shapes, when ‘small’ particles are considered. Similarly, tetrahedral or hexagonal shapes have higher energies than Mackay, Marks, and truncated octahedral (TO). The energetics relative energetics show that the latter three shapes are most relevant for the understanding of the

interplay of bulk, surface, and strain effects in observed particle shapes, especially under equilibrium or closet-to equilibrium conditions. Examples of Mackay, Marks and TO shapes are shown in Figure 1.

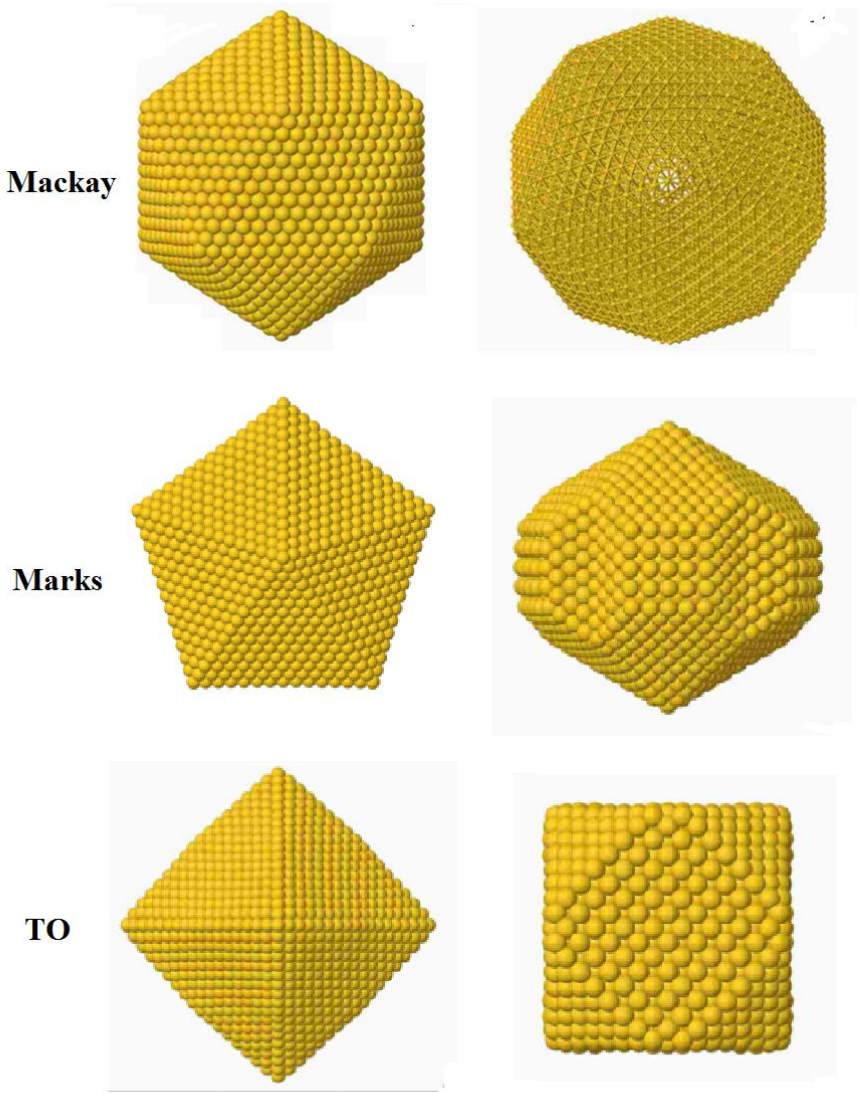

Figure 1. ***top:*** Mackay (or icosahedral, Ih, N=12) gold nanoparticles. The more atoms are contained in the particle, the more spherical it appears. The Mackay cluster on the left-hand side has 3871 atoms, while the larger particle on the right-hand side has 5083 atoms. ***middle:*** Marks (or decahedral) gold nanoparticles [15,1,1]; untruncated top view (left)and [5,5,5] truncated (right). The un-truncated particle has 2815 atoms while the truncated has 2987 atoms in the cluster. Notation adopted from Balleto *et al.* [18] ***bottom:*** Octahedral gold nanoparticles. [18,0]: not truncated (left) and [18,9]: truncated (right). The octahedral particle contains 2894 atoms while the truncated has 2184 atoms. Notation adopted from Baletto *et al.* [18] (Color Online)

Mackay (or icosahedral, Ih) clusters consists of 20 distorted (111)-like facets, and they are attractive since they approach a semi-spherical shape for larger particle sizes.[16] Mackay cluster exhibit five-fold symmetry and optimize the surface energy due to slightly distorted (111) surface facets, but this comes at the expense of large internal strain propagating throughout the whole volume. Therefore, icosahedral clusters are found to be stable for small cluster sizes of up to ~100 atoms.

Marks (or decahedral, Dh, *bco)* clusters can be formed from two pentagonal pyramids with a shared base. [17] The decahedral particle is built out of five tetrahedra sharing a common five-fold rotation axis. These tetrahedra are slightly distorted to achieve space filling. Marks clusters exhibit less internal strain compared to Mackay clusters, but expose energetically unfavorable (100) facets in simple rectangular truncation. However, part of the high (100) surface energy can be recovered by forming (111) like re-entrance surfaces that if present can lead to non-convex shape of the particles (see Figure 1 middle, right). We find that Marks clusters might be stable for some intermediate cluster sizes up to ~500 atoms. For the remainder of this paper, we will refer to the Marks clusters as *bco* type.

'Larger' gold clusters are predicted to form truncated octahedral shapes (TO). The TO structure minimizes the internal strain but expose unfavorable (100) facets (Fig. 3, right). General scaling of surface the area/volume ratio scales as 1/R, where R is the size of the particle. Thus, strain reduction in the particle volume will compensate for the increase of unfavorable surface area and TO clusters are expected to be stable for sufficiently large clusters, in agreement with our as well as previous computations using different sets of effective potentials. The ratio of (100) and (111) surface energy for Au is in the range of 1.15 [18] to 1.36 [19], we find a ratio of 1.35. Importantly, the ratio is larger than 1 and (100) surfaces are energetically unfavorable and a finite minimum particle size is needed to stabilize TO shaped particles. TO clusters are expected to be the equilibrium shape in the macroscopic limit (10^4 atoms or so), beyond which spherical *fcc* particles are expected. [9]

The results of our equilibrium GLUE computations for gold nanoparticles are in excellent agreement for Mackay, Marks, and TO compare very well with the previous findings by Baletto *et al.* [18]

3. Non-equilibrium CVD growth of gold nanoparticles

Decahedral gold nanoparticles used for this study were grown using CVD onto a silicon substrate with the native oxide in a catalyst-free thermal approach with $AuCl_3$ as a precursor. Powdered $AuCl_3$ was loaded in a Ni boat, placed in a quartz tube annealed at 475°C for approximately one hour under an Ar carrier-gas flow. [7] Through this process, nanocrystals form without the use of a catalyst, which often introduces unwanted chemical heterogeneities. This approach is similar to the protocol that was used successfully to synthesize Ni nanocrystals [20,21] and yields single-crystal gold nanocrystals with well-defined facets (see Figs. 4). In contrast, other synthesis techniques for gold nanocrystals rely on surfactants to control shape and/or size. Our synthesis protocol can be used to create many different shapes of gold nanocrystals, ranging from spherical, triangular plates and octahedra to multiple twinned particles such as decahedra and icosahedra. These equilibrium nanocrystal shapes can be understood by employing the Wulff construction [22] that relates lower surface energies to larger surface areas.

Aside from nanocrystals enclosed by identical polygonal surfaces, CVD synthesis may also result in some triangular plate-like crystals, which are believed to be a result of stacking faults. [24,25] If the planar seed exhibits a stacking fault, gold atoms added near the fault give rise to crystal growth [Germain2003, Lofton2005]. Regardless of this difference in process of formation, gold nanocrystals with both triangular plate and octahedral shapes retain some of the symmetries inherent to the *fcc* unit cell. [26] As can be seen in Figure 2, some of the polyhedral-shaped gold nanocrystals grow to surprisingly large sizes, ranging from a few nanometers up to microns, under the non-equilibrium CVD growth conditions, which is inconsistent with the stability predictions from theory. Recently, some of these large-sized polyhedral gold nanocrystals were studied by coherent X-ray diffraction [27], but some details of their local structure have remained to be a mystery.

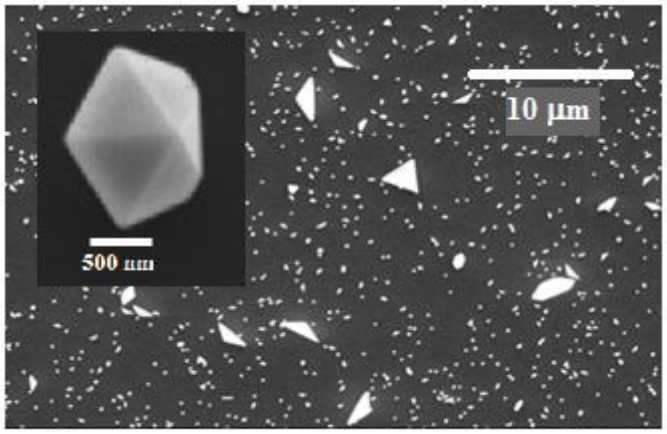

Figure 2. Scanning Electron Microscopy (SEM) picture of CVD-grown gold nanoparticles on Si/SiO_2 substrate. One observes a variety of nanoparticle shapes spanning the sub-nanometer to the micron scale in sizes. In the insert at upper-left corner, a close-up of a 'very large' decahedral particle is shown.

4. Simplistic Models of Decahedral Nanoparticles

A regular decahedron was chosen to be the representative of five-fold twinned gold nanoparticles for purposes of creation of different models. Four simplistic computer models were created, consistent with three proposed lattice structures of the decahedral particles: model 1: an undistorted *fcc* lattice with single gap (pseudo-five-fold symmetry); model 2: an undistorted *fcc* lattice with a distributed gap exhibiting five-fold symmetry, model 3: a distorted, spatially continuous particle with *bco* lattice exhibiting five-fold symmetry; and model 4: a hybrid contained three distorted *bco* and two undistorted *fcc* subunits.

In order to generate twinned fcc-type particles with a gap (models 1 and 2), we constructed a tetrahedral shape from the bulk *fcc* lattice by cutting along the (111) planes of the (conventional) *fcc* lattice, which result in tetrahedral subunits with an opening angle of 70.54^o for an undistorted *fcc* lattice.

For model 1, the parent tetrahedral *fcc* subunit is then rotated about the [110] direction such that the sides of the subunits meet in a contact plane. Assuming no lattice distortion, the resulting particle exhibits a spatial discontinuity due to failure of the five rotations to span 360°, and it results in a twinned *fcc*-type decahedron with a 7.35^o wedge of missing atoms. This missing solid wedge may be referred to as a spatial discontinuity or disclination (broken rotational symmetry). For model 2, the tetrahedral *fcc* subunit is rotated by 72°, thus leaving five smaller gaps of about

1.5^{o} between adjacent subunits. A problem with both undistorted models 1 and 2 is that recent high-resolution transmission-electron microscopy (HR-TEM) studies by Johnson *et al.* on a decahedral gold particle show no evidence for gap (or wedges of missing material) between tetrahedral subunits [30], which is also expected from the energy gained through bond formation upon gap closure. However, there are two possible ways to avoid the opening of a larger gap: a) once the gap has opened far enough, an additional plane of atoms is inserted into the gap, and that process is repeated until the particle boundary is reached, or b) cubic lattices are prone to twinning along the (111) directions, thus the connecting faces may consist of twin boundaries that are more flexible of accommodating the (small) additional strain locally without affecting the interior of the particle. Decahedral particles with twin boundaries at the connecting faces will no longer have a common rotation axis. Data by Johnson *et al.* seem more consistent with the latter, i.e. heterogeneous strain distribution at the connecting faces of the multiply-twinned gold nanoparticles. [30]

Model 3 is driven by the desire to create a uniform particle, in which a five-fold rotation spans all of 360°, and this requires slight lattice distortion along one dimension. The distorted parent unit is then rotated about [110] such that a spatially continuous particle results. Model 3 exhibits the same geometrical relationships compared to a particle formed by shell accumulation considering five-fold symmetry to begin with, using a pentagonal packing scheme as originally proposed by Bagley. [31] The tetrahedral subunits are no longer equilateral; the angle between two of the sides increases to 72°, such that five-fold twinning about the [110] axis spans exactly 360°. While symmetry is lost for each of the five subunits, additional symmetry is gained for the particle as a whole, the model-3 particle has a true five-fold symmetry. In essence, this model results in a transformation of crystal class from face-centered cubic (*fcc*) to body-centered orthorhombic (*bco*). It should be noted that the packing density of the resulting *bco* structure is still larger than that for hexagonal closed packed (*hcp*). [31]

Model 4 is a hybrid structure comprised of tetrahedral subunits of both undistorted *fcc* and distorted *bco* subunits, for example, three distorted subunits with a *bco* symmetry (with an angle of ~73°) and two with undistorted *fcc* symmetry. The possibility of a hybrid model was supported by observation of such hybrid model for indium nanoparticles. [Chen1999]

The software used to construct these computer models is the DISCUS program. [28,29] Given space group, lattice parameter, atomic positions within the unit cell, and the total number of unit cells desired in the structure, DISCUS will generate an initial structure and the structure can then be modified by specifying the boundaries or surfaces desired. Example sketches of decahedral gold nanoparticles for the four different models are shown in Figure 3.

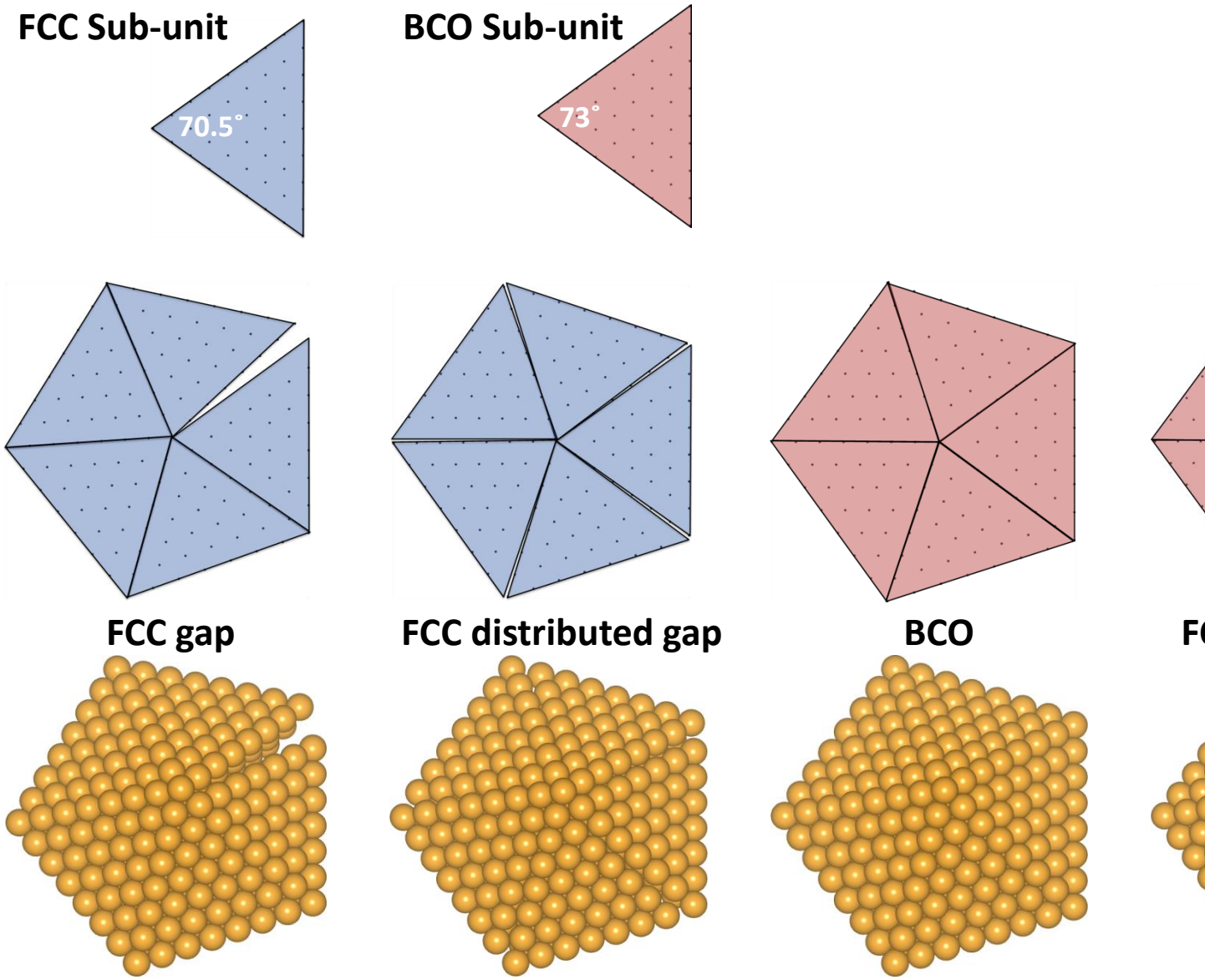

Figure 3. Construction of decahedral gold nanoparticles using four different models; from left to right: a) undistorted fcc-type particle with a single gap, b) undistorted *fcc*-type particle with a

distributed gap, c) distorted bco-type particle and d) hybrid structure (see text for more explanation). (Color Online)

5. Limitations of Bragg Diffraction

Although any physical crystal is finite, the crystals must be of sufficient size to generate a meaningful diffraction pattern. Standard diffraction techniques make use of the Bragg condition, which states that constructive interference occurs when the path difference $2d\ sin\theta$ between sets of parallel planes of scatterers is an integer multiple of the wavelength λ of the incident beam. Macroscopic particles contain a large enough number of crystallographic planes with scatterers, and therefore the intensity observed from constructively interfering scattered waves results in relatively sharp, narrow, well-defined peaks. However, as the particle size decreases, peaks will broaden due to the inverse relationship between features of a diffraction pattern and features of the object responsible for the pattern: decreased size of a particle in direct space is associated with increased width of its diffraction image in reciprocal space. With increasing width, the peaks become more difficult to resolve and therefore provide less meaningful information about the real-space object. Some peaks may disappear altogether because there are no longer enough scatterers to create a set of parallel planes with interplanar spacings responsible for those peaks. Bragg peaks will experience broadening due to instrument resolution and additional broadening due to internal strains and/or its particle size, as outlined above. A commonly used software package for diffraction studies is the General Structure Analysis System (GSAS) [33,34], and it allows simulating the effect of particle-size broadening on the peak profiles for a given instrument-parameter file. In GSAS, the parameter responsible for particle-size is known as σ_2, and it is inversely proportional to the particle size with

$$\sigma_2 = \sqrt{\frac{(CK/p)^2}{8\ ln2}}, \tag{1}$$

where p is the average particle diameter, C the instrument-specific diffractometer constant and K the Scherrer constant (typically ~1).

In Figure 4, we show the effects of particle-size broadening for gold nanoparticles, using equation (1) with the instrument-parameter file of the high-resolution powder diffractometer NPDF, a high-resolution neutron powder diffractomer that was dedicated to pair-distribution-

function studies (see below) and operated as a user instrument at the Los Alamos Neutron Science Center (LANSCE) until 2016. It is apparent that particle-size broadening is insignificant for micron-sized particles, reasonable (although with significantly reduced intensity) diffraction patterns can be obtained for particles as small as 10 nm, while the analysis diffraction patterns for smaller particles is essentially featureless. Therefore, the analysis in terms of Bragg diffraction has severe limitations when it comes to very small particles.

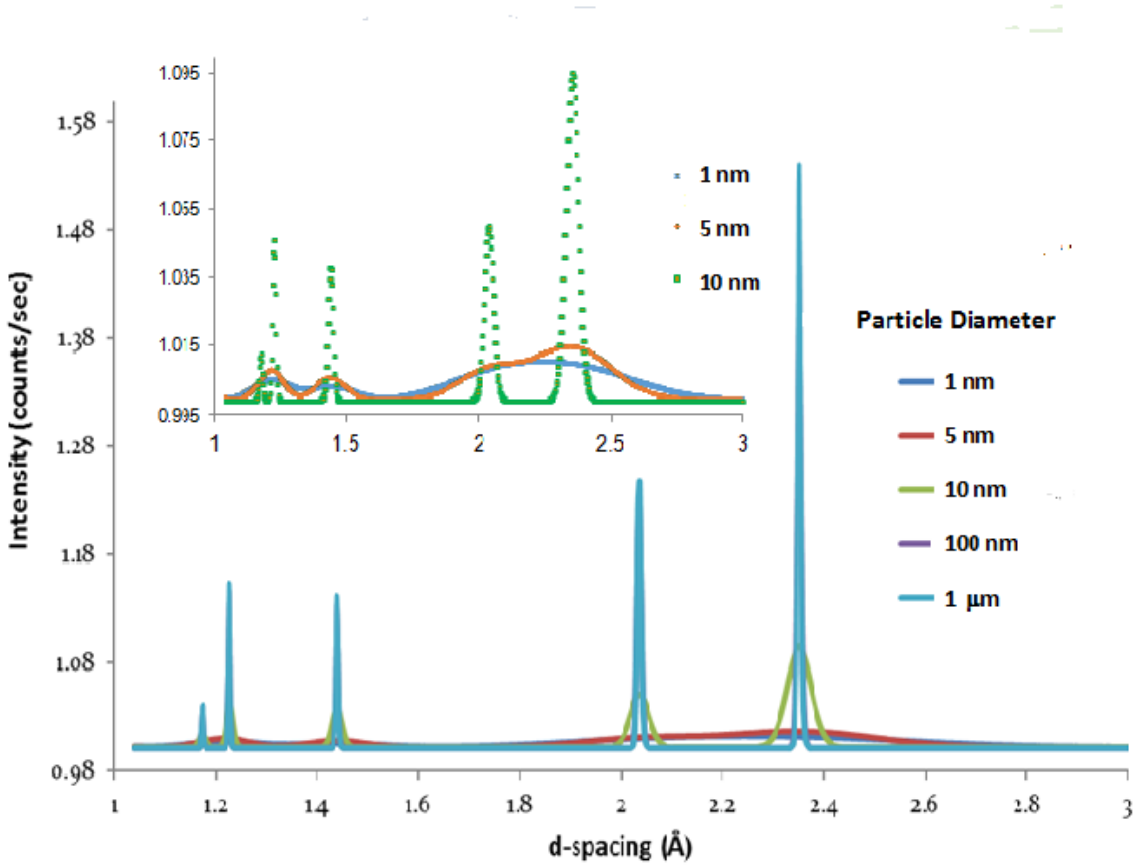

Figure 4. Simulated powder diffraction patterns as a function of *d* spacing for gold nanoparticles of different sizes. The insert exemplifies the severe particle-size peak broadening for particles below 10 nm. The background is set at 1. (Color Online)

7. Pair Distribution Function Analysis

As shown in the previous section, traditional diffraction techniques have limitations when particles become nanosized. Moreover, detection of local disorder is generally beyond the scope of diffraction techniques altogether since diffraction techniques provide a bulk average and therefore convey average structural parameters. However, unlike liquids and amorphous

materials, which tend to have only short-range structural correlations, nanoparticles tend typically exhibit some form of long-range order, but it is not necessarily described in terms of a Bravais lattice. For example, the five-fold symmetry of decahedral particles violates translational symmetry, even though some rotational symmetry may be preserved. In some cases, the symmetry of such particles is actually pseudosymmetric, for example for particles with a gap or a small spatial discontinuity. Particles with a true five-fold symmetry are referred to as quasi-crystals as they still lack the translational periodicity associated with a Bravais lattice. [35]

Pair distribution function (PDF) analysis provides a statistical description of a structure rather than a determination of the specific atomic configuration. Moreover, PDF studies do not rely on any principles of crystallographic symmetries. [36] This technique was originally introduced for studies of liquids or amorphous materials, which are dominated by short-range structural correlations. More recently, PDF studies have also been applied to crystalline solids with disordered regions or nanosized crystalline materials [37-40], where traditional diffraction techniques can no longer provide the desired local-structure information. Typically, PDF analysis in such materials identifies deviations from the expected (known) bulk configurations.

The PDF is connected to the likelihood to find an atom at a certain distance from any given atom. One can define a *pair-correlation function* $g(\boldsymbol{r},\boldsymbol{r'})$, which is related to the probability $P^{(2)}(\boldsymbol{r},\boldsymbol{r'})$ of independently finding an atom at position $\boldsymbol{r}$ and another at position $\boldsymbol{r'}$ with the averages of the respective densities $\rho(\boldsymbol{r})$ and $\rho(\boldsymbol{r'})$:

$$\boldsymbol{g}\left(\vec{\boldsymbol{r}},\vec{\boldsymbol{r'}}\right)\left[\langle\boldsymbol{\rho}(\vec{\boldsymbol{r}})\rangle\boldsymbol{\rho}\left(\vec{\boldsymbol{r'}}\right)\right] = \boldsymbol{P}^{(2)}\left(\vec{\boldsymbol{r}},\vec{\boldsymbol{r'}}\right) = \langle\sum_{j=1}^{N}\boldsymbol{\delta}\left(\vec{\boldsymbol{r}}-\vec{\boldsymbol{R}_j}\right)\sum_{k=1}^{N}\boldsymbol{\delta}\left(\vec{\boldsymbol{r'}}-\vec{\boldsymbol{R}_k}\right)\rangle. \tag{2}$$

This is equal to the probability of finding two atoms that are separated by a distance $\boldsymbol{R} = \boldsymbol{R_j} - \boldsymbol{R_k}$, where $\boldsymbol{R_j}$ and $\boldsymbol{R_k}$ are summed over all atom positions in the material. For a particle of volume V and one type of atoms, the full pair-correlation function can then be determined by integrating over the whole volume with proper normalization:

$$\boldsymbol{g}\left(\vec{\boldsymbol{r}},\vec{\boldsymbol{r'}}\right)\langle\boldsymbol{\rho}\rangle^2 = \frac{1}{V}\int\left[\sum_{j=1}^{N}\boldsymbol{\delta}\left(\vec{\boldsymbol{r}}-\vec{\boldsymbol{R}_j}\right)\sum_{k\neq j}^{N}\boldsymbol{\delta}\left(\vec{\boldsymbol{r'}}-\vec{\boldsymbol{R}_k}\right)\right]\boldsymbol{d}^3\boldsymbol{r'}. \tag{3}$$

Experimentally, one cannot measure the pair correlation function directly. After correction/normalization of the measured intensities for external (e.g. background, detector efficiency, incident spectrum) and internal (e.g. incoherent scattering) contributions, one can

determine the structure function $S(\boldsymbol{Q})$, which provides the total scattering response of the N atoms of the whole sample:

$$\boldsymbol{S}(\vec{\boldsymbol{Q}}) = \frac{\boldsymbol{1}}{\boldsymbol{N}} \int \sum_{\boldsymbol{j=1}}^{\boldsymbol{N}} \boldsymbol{\delta}(\vec{\boldsymbol{r}} - \vec{\boldsymbol{R}}_{\boldsymbol{j}}) \boldsymbol{e}^{\boldsymbol{i}\vec{\boldsymbol{Q}}\cdot\vec{\boldsymbol{r}}}\, \boldsymbol{d}^{\boldsymbol{3}}\boldsymbol{r} \int \sum_{\boldsymbol{k=1}}^{\boldsymbol{N}} \boldsymbol{\delta}(\vec{\boldsymbol{r}'} - \vec{\boldsymbol{R}}_{\boldsymbol{k}}) \boldsymbol{e}^{\boldsymbol{i}\vec{\boldsymbol{Q}}\cdot\vec{\boldsymbol{r}'}}\, \boldsymbol{d}^{\boldsymbol{3}}\boldsymbol{r}' \,, \tag{4}$$

where $\boldsymbol{Q} = \boldsymbol{k_i} - \boldsymbol{k_f}$ is the scattering vector, determined by the difference of the incident and scattered wave vectors. In other words, the structure function measures the combined response of all atoms, not limited to pairs of atoms. However, it can be easily shown that the structure function is related to the pair correlation function *via*:

$$\boldsymbol{S}(\vec{\boldsymbol{Q}}) = \boldsymbol{1} + \frac{\boldsymbol{1}}{\boldsymbol{N}} \int \boldsymbol{V}\langle\boldsymbol{\rho}\rangle^{\boldsymbol{2}}\, \boldsymbol{g}(\vec{\boldsymbol{R}}) \boldsymbol{e}^{\boldsymbol{i}\vec{\boldsymbol{Q}}\cdot\vec{\boldsymbol{R}}} \boldsymbol{d}^{\boldsymbol{3}}\boldsymbol{R}. \tag{5}$$

The '1' in equation (4) represents the self-correlation term of each atoms with itself. After subtracting this self-correlation term, one can invert equation 5 with an inverse Fourier transformation.

One can define a new quantity $G(\boldsymbol{R})$:

$$\boldsymbol{G}(\vec{\boldsymbol{R}}) = \boldsymbol{4\pi R}\,\langle\boldsymbol{\rho}\rangle\,[\boldsymbol{g}(\vec{\boldsymbol{R}}) - \boldsymbol{1}] = \frac{\boldsymbol{2}}{\boldsymbol{\pi}} \int_{\boldsymbol{0}}^{\infty} \vec{\boldsymbol{Q}}[\boldsymbol{S}(\vec{\boldsymbol{Q}}) - \boldsymbol{1}] \boldsymbol{sin}(\vec{\boldsymbol{Q}} \cdot \vec{\boldsymbol{R}}) \boldsymbol{dQ}, \tag{6}$$

which provides a measure of correlations between an atom at the center of a sphere and atoms on the surface of a spherical shell with area $4\pi R^2$ and thickness dR.

The determination of $G(R)$ critically depends on the accurate determination of $S(Q)$ *via* equation (6). However, this equation contains an integral over dQ from 0 to ∞, and it is obviously impossible to reach infinity experimentally (as well as computationally) and thus there has to be a cut-off Q_{max}. The results are so-called *Fourier ripples* (or fluctuations) due to shortened Fourier transforms. Since PDF signals tend to be small, one requires high maximum-momentum transfer Q_{max}, because of the convolution of $G(R)$ with $sin(Q_{max}\, R)/R$. In addition, one requires good Q resolution, because the PDF is damped by $exp[-(r\Delta Q)^2/2]$. Finally, PDF instruments should have good counting statistics and resolution as well as low (and stable) backgrounds, including incoherent scattering.

PDF experiments can therefore provide a quantitative measurement of the relative abundance of atom-atom pair distances within a material regardless of symmetry and absence of long-range order. In principle, a PDF analysis evaluates only distances, resulting in a one-dimensional

function. However, a three-dimensional structure can often be inferred from comparison of PDF data when combined with model calculations. This approach allows identifying all interatomic distances and deviations from periodicity present in a material.

8. Model PDFs and Diffraction Patterns and Comparison with Experiments

Model PDFs and diffraction for the four models and a bulk *fcc* sphere were computed using the program packages TOPAS V6 and DShaper. [41,42]

To see whether PDF studies exhibits sufficient sensitivity to distinguish between different models, we first computed the PDFs of our four models in comparison with a bulk spherical *fcc* gold particle. For the computations, we used the instrument specifications for the 11-IDB instrument, (used for the experiments) which is a high-energy beam line at the Advanced Photon Source, Argonne National Laboratory. Its resolution is typically no better than 5% in the 5 Å range and Q_{max} of the instrument is 30 $Å^{-1}$. The models were labeled as follows: bulk *fcc* spherical particle – FCC sphere; unstrained *fcc*-type with a single 7.35^{o} gap - FCC gap, unstrained *fcc*-type with five distributed 1.5^{o} gaps between all tetrahedral units - FCC dist. gap, strained *bco*-type - BCO, and hybrid type -BCO/FCC hybrid.

Example results for very small particles of ~430 atoms for each of the models are shown in Figure 5.

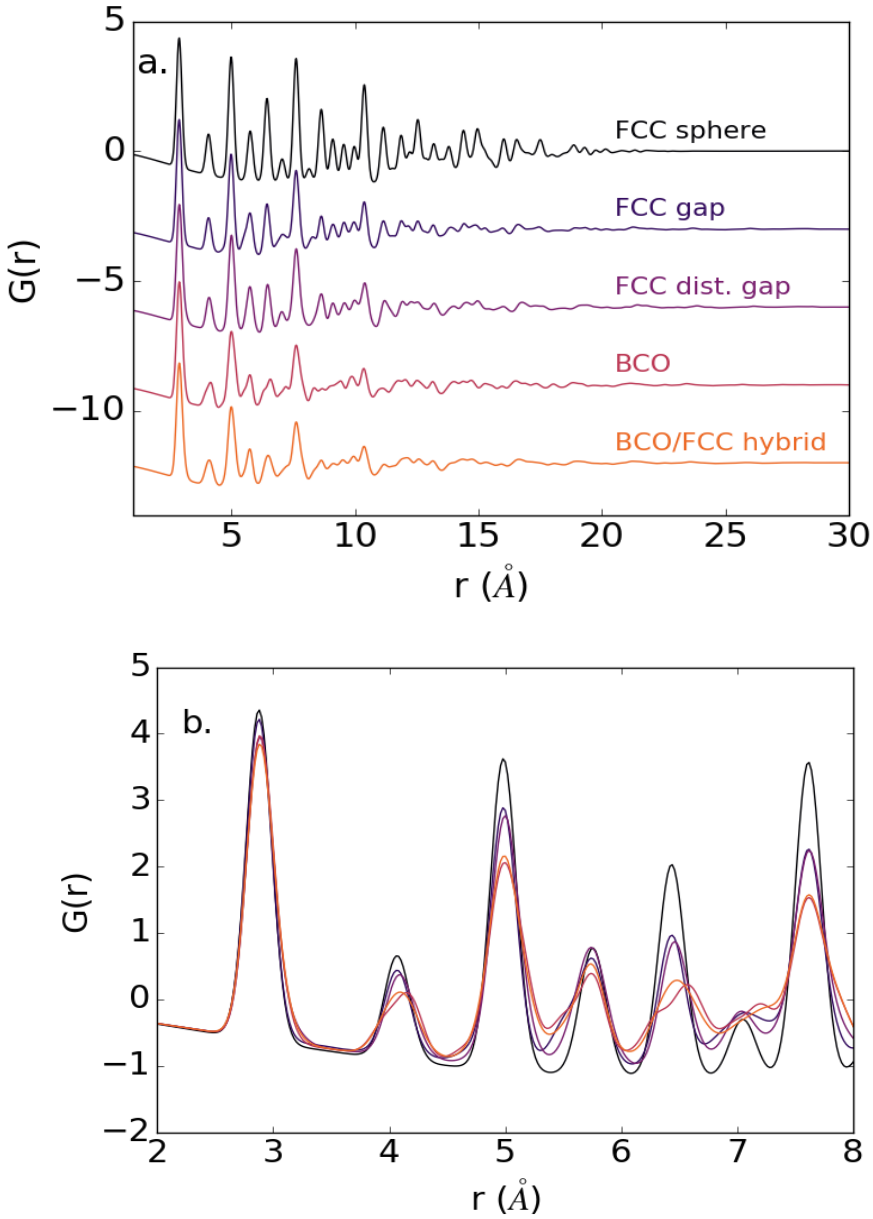

Figure 5. Comparison of simulated model PDFs for small gold particles, containing ~430 atoms and a size less than 2 nm, shown a) across their full range to 30 Å in real space and b) in more detail out to 8 Å in real space. The model PDFs presented here are: a bulk *fcc* sphere and the four decahedral nanoparticle models shown in Figure 3. In a), the *G(r)*'s for the different models are shifted for clarity. (Color Online)

We computed PDFs for particles of various sizes, and we find that the models can be readily distinguished at all sizes (see supplementary information).

This is in contrast to the computed response from X-ray diffraction, where distinction between different models may be impossible for small particle sizes, as already outlined in section 5. In Figure 6, we show the model diffraction patterns for the same model particles used for PDF computations presented in Figure 5.

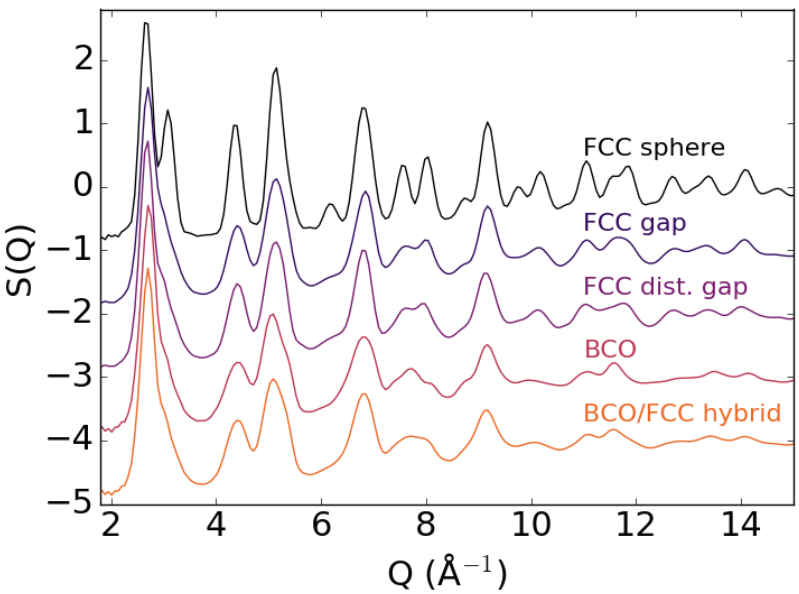

Figure 6. Comparison of simulated diffraction patterns for an *fcc* sphere model and the four different decahedral nanoparticle models in Figure 3. The *S(Q)*'s for the different models are shifted for clarity. (Color Online)

It is apparent the diffraction patterns for the different models look similar for small particle sizes, particularly for the stronger peaks. Therefore, distinction between different models becomes ambiguous at least. For larger particle sizes (above 10 nm or so), however, diffraction results may provide such information (see supporting information).

Finally, we decide to test some of our model predictions for PDFs and diffraction patterns with experimental data that were collected on 11-IDB on a fairly large 17-nm decahedral gold nanoparticle. The experimental PDF of the 17-nm particle was computed using the software package PDFgetX3. [43.44]

Our comparison focused on two 'large' decahedral models (~53,300 atoms, largest dimension ~18 nm): the *fcc*-type model with the distributed gap (model 2, FCC dist. gap) and the *bco*-type model (model 3, BCO). If an unstrained *fcc*-type structure forms, it seems reasonable to expect that the gap is more likely distributed over five smaller gaps, thereby reducing the demands on strain at the connecting interfaces of the tetrahedral subunits. The hybrid structure (model 4) would be expected to show signatures of the *bco*-type particles, since three out of the five subunits are *bco*-type. The results are shown in Figure 7.

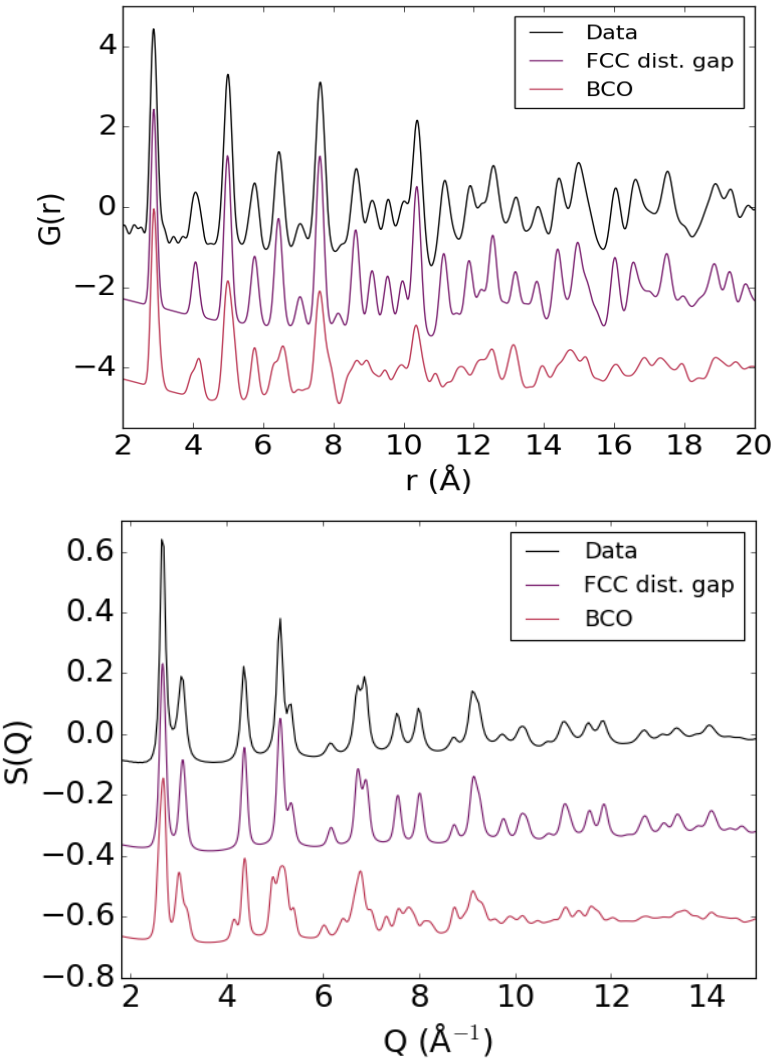

Figure 7. Comparison of experimental PDF data (top) and diffraction data (bottom) for 17-nm decahedral gold particles (labeled DATA) with model predictions for an unstrained *fcc*-type distributed gap decahedral gold particle (FCC dist. gap) and a strained *bco*-type decahedral godl particle (BCO). The instrument parameters in the simulations were adjusted to replicate the experimental settings. (Color Online)

For both data sets, PDF and diffraction, the experimental data matches the predictions of the *fcc*-type distributed gap model very well, while there is poor agreement with the *bco*-type model. In fact, the experimental data seem to exclude any significant strained *bco*-type contributions, thereby eliminating hybrid structures as a possible model.

9. Conclusions

Under non-equilibrium CVD-growth conditions, facetted gold particles grow to sizes much larger than expected from equilibrium atomistic calculations. The modeling of five-fold decahedral gold nanoparticles involves significant uncertainty in that there various approaches have been proposed on how to assemble the decahedral particle, such as unstrained *fcc*-type structures with a gap (either a single gap or a distributed one), strained *bco*-type structures and *hybrid* structures. Our findings provide evidence that the strained *bco*-type and hybrid models are inadequate for the description of our studied 17-nm decahedral gold nanoparticle, while an unstrained *fcc*-type model with a distributed gap provides excellent agreement with the experimental result. It seems reasonable to assume that the energies due to bulk strains are likely prohibitively high for the formation of large polyhedral nanoparticles. On the other hand, even the fcc-type decahedral gold particles cannot be completely unstrained given that no gaps or additional layers of atoms could be discerned in the HR-TEM work by Johnson *et al.* [30] We speculate that the strains are limited to contact surfaces of the tetrahedral subunits. An estimate of the number of atoms in gapped unstrained 17-nm *fcc*-type decahedral particle compared to one without a gap reveals that there are less than 2% of missing atoms. Therefore, their contributions to the experimental PDF are too weak to be resolved.

More generally, we have shown that studies using a combination of atomistic models, X-ray PDF and diffraction techniques provide insight into the local structure of nanoparticles that is complementary to TEM or similar techniques, although the instrument and sample-preparation requirements can be very challenging, considering sampling sizes, Q range and resolution in addition to the often notoriously difficult background corrections.

Acknowledgements

CVD growth and SEM characterization of the gold nanoparticles occurred in the UCSD's Fullerton Laboratory, with is supported by a grant from the National Science Foundation (Award Number: DMR-0906957).

This work has benefitted from the use of Advanced Photon Source at Argonne National Laboratory which is supported by the U.S. Department of Energy, Office of Science, Office of Basic Energy Sciences, under Contract No. DE-AC02-06CH11357.

Data simulations and comparison with experimental data were supported through the U.S. Department of Energy, Office of Science, Office of Basic Energy Sciences, Early Career Research Program, Award No. KC040602, under contract no. DE-AC05-00OR22725.

References

[1] Clavero C 2014 Plasmon-induced hot-electron generation at nanoparticle/metal-oxide interfaces for photovoltaic and photocatalytic devices *Nature Photonics* **8** 95-103

[2] Homberger M and Simon U 2010 On the application potential of gold nanoparticles in nanoelectronics and biomedicine *Phil. Trans. R. Soc. A* **368** 1405–1453[3] Cao Y C, Jin R and Mirkin C A 2002 Nanoparticles with Raman spectroscopic fingerprints for DNA and RNA detection *Science* **297** 1536-1540

[4] Huang X, El-Sayed I H, Qian W and El-Sayed M A 2006 Cancer Cell Imaging and Photothermal Therapy in the Near-Infrared Region by Using Gold Nanorods *J. Am. Chem. Soc.* **128** 2115-2120

[5] Li C Z, Male K B, Hrapovic S and Luong J H T 2005 Fluorescence properties of gold nanorods and their application for DNA biosensing *Chem. Commun.* **31** 3924-3926

[6] Sudeep P K, Joseph S T S and Thomas K G 2005 Selective Detection of Cysteine and Glutathione Using Gold Nanorods *J. Am. Chem. Soc.* **127** 6516-6517

[7] Ghosh S K and Pal T 2007 Interparticle Coupling Effect on the Surface Plasmon Resonance of Gold Nanoparticles: From Theory to Applications *Chem. Rev.* **107** 4797-4862

[8] Kelly K L, Coronado E, Zhao L L and Schatz G C 2003 The Optical Properties of Metal Nanoparticles: The Influence of Size, Shape, and Dielectric Environment *J. Phys. Chem.* B **107** 668-677

[9] Manna S, Kim J W, Takahashi Y, Shpyrko O B and Fullerton E E 2016 Synthesis of single-crystalline anisotropic gold nano-crystals via chemical vapor deposition *J. Appl. Phys.* **119** 174301

[10] Hofmeister H 2004 Fivefold Twinned Nanoparticles, in E*ncyclopedia of Nanoscience and Nanotechnology* Vol.3 ed. H S Nalwa (Valencia CA: American Scientific Publishers) 431-452

[11] Qian X and Park H S 2010 The influence of mechanical strain on the optical properties of spherical gold nanoparticles *J. Mech. Phys. Solids* **58** 330-345

[12] Baletto F and Ferrando R 2005 Structural properties of nanoclusters: Energetic, thermodynamic, and kinetic effects *Rev. Mod. Phys*. **77** 371-423

[13] Ercolessi F, Parrinello M and Tosatti E 1988 Simulation of Gold in the Glue Model *Phil. Mag A* **58** 213-226

[14] Gale J D 1997 GULP: A computer program for the symmetry-adapted simulation of solids. *J. Chem. Soc, Faraday Trans***. 93** 629-637

[15] Gale J D and Rohl A 2003 The General Utility Lattice Program (GULP). *Mol. Simulat.* **29** 291-341.

[16] Mackay A L 1962 A dense non-crystallographic packing of equal spheres *Acta Cryst.* **15** 916-918

[17] Marks L D 1984 Surface structure and energetics of multiply twinned particles *Phil Mag A* **49** 81-93

[18] Baletto F, Ferrando R, Fortunelli A, Montalenti F and Mottet C 2002 Crossover among structural motifs in transition and noble-metal clusters *J. Chem. Phys.* **116** 3856-3863

[19] Galanakis I, Bihlmayer G, Bellini V, Papanikolaou N, Zeller R, Blugel S, Dederichs P H 2002. Broken-bond rule for the surface energies of noble metals *Europhys. Lett.* **58** 751-757

[20] Chan K T, Kan J J, Doran C, Ouyang L, Smith D J and Fullerton E E 2010 Oriented growth of single-crystal Ni nanowires onto amorphous SiO_2 *Nano Lett.* **10** 5070-5075

[21] Fohtung E, Kim J E, Chan K T, Harder R, Fullerton E E and Shpyrko O G 2012 Probing the three-dimensional strain inhomogeneity and equilibrium elastic properties of single crystal Ni nanowires *Appl. Phys. Lett.* **101** 033107

[22] Wulff G 1901 Zur Frage der Geschwindigkeit des Wachstums und der Auflösung der Krystallflächen *Z. Krystallogr. Mineral.* **34**, 449-530

[23] Wang Z L 2000 Transmission Electron Microscopy of Shape-Controlled Nanocrystals and Their Assemblies *J. Phys. Chem. B* **104** 1153-1175

[24] Germain V, Li J, Ingert D, Wang Z L and Pileni M P 2003 Stacking Faults in Formation of Silver Nanodisks *J. Phys. Chem. B* **107** 8717-8720

[25] Lofton C and Sigmund W 2005 Mechanisms Controlling Crystal Habits of Gold and Silver Colloids *Adv. Funct. Mater.* **15** 1197-1208

[26] Sun Y and An C 2011 Shaped gold and silver nanoparticles *Front. Mater. Sci.* **5** 1-24

[27] Kim J W, Manna S, Dietze S H, Ulvestad A, Harder R, Fohtung E, Fullerton E E and Shpyrko O G 2014 Curvature-induced and thermal strain in polyhedral gold nanocrystals *Appl. Phys. Lett.* **105** 173108

[28] Proffen T and Neder R B 1997 DISCUS: a program for diffuse scattering and defect-structure simulation *J. Appl. Cryst.* **30** 171-175

[29] Proffen T and Neder R B 1999 DISCUS: a program for diffuse scattering and defect-structure simulation - Update *J. Appl. Cryst.* **32** 838-839

[30] Johnson C L, Snoeck E, Ezcurdia M, Rodriguez-González B, Pastoriza-Santos I, Liz-Marzán L M and Hÿtch M J 2008 Effects of elastic anisotropy on strain distributions in decahedral gold nanoparticles *Nature Materials* **7** 120-124

[31] Bagley B G 1965 A Dense Packing of Hard Spheres with Five-fold Symmetry *Nature* **208** 674-675

[32] Chen Q, Tanaka M and Furuya K 1999 Unusual crystallographic structure and its fluctuation of indium nanoparticles as-deposited and observed with HRTEM using the UHV-DC-TEM system *Surf. Sci.* **440** 398-406

[33] Larsen A C and Von Dreele R B 2000 General Structure Analysis System (GSAS) *Los Alamos National Laboratory Report* LAUR 86-748

[34] Toby B H 2001 EXPGUI, a graphical user interface for GSAS *J. Appl. Cryst.* **34** 210-213

[35] Hammond C 2009 The Basics of Crystallography and Diffraction, 3rd Ed. (New York; Oxford University Press) pp 127-130

[36] Toby B H and Egami T 1992 Accuracy of pair distribution function analysis applied to crystalline and non-crystalline materials *Acta Cryst.* **A48** 336-346

[37] Page K, Proffen T, Terrones H, Terrones M, Lee L, Yang Y and Cheetham A K 2004 Direct observation of the structure of gold nanoparticles by total scattering powder neutron diffraction *Chem. Phys. Lett.* **393** 385-388

[38] Page K, Hood TC, Proffen T and Neder R B 2011 Building and refining complete nanoparticle structures with total scattering data *J. Appl. Cryst.* **44** 327-336

[39] Wang H W, Wesolowski D J, Proffen T E, Vlcek L, Wang W, Allard L F, Kolesnikov A I, Feygenson M, Anovitz L M and Paul R L 2013 Structure and Stability of SnO_2 Nanocrystals and Surface-Bound Water Species *J. Am. Chem. Soc*. **135** 6885– 6895

[40] Liu J, Olds D, Peng R, Yu L, Foo G S, Qian S, Keum J, Guiton B S, Wu Z and Page K 2017 Quantitative analysis of the morphology of {101} and {001} faceted anatase TiO_2 nanocrystals and its implication on photocatalytic activity *Chem. Mat.* (in press)

[41] Coelho A, Chater P and Kern 2015 Fast Synthesis and Refinement of the Atomic Pair Distribution Function *J. Appl. Cryst.* **48** 869−875

[42] Olds D, Wang H W and Page K 2015 DShaper: An Approach for Handling Missing Low-Q Data in Pair Distribution Function Analysis of Nanostructured Systems *J. Appl. Cryst.*. **48** 1651−1659

[43] Chupas P J, Chapman K W and Lee P L 2007 Applications of an amorphous silicon-based area detector for high-resolution, high-sensitivity and fast time-resolved pair distribution function measurements *J. Appl. Cryst.* ***40*** 463-470

[44] Juhás P, Davis T, Farrow C L and Billinge S J 2013 PDFgetX3: a rapid and highly automatable program for processing powder diffraction data into total scattering pair distribution functions *J. Appl. Cryst.* **46** 560-566

Supplementary Information

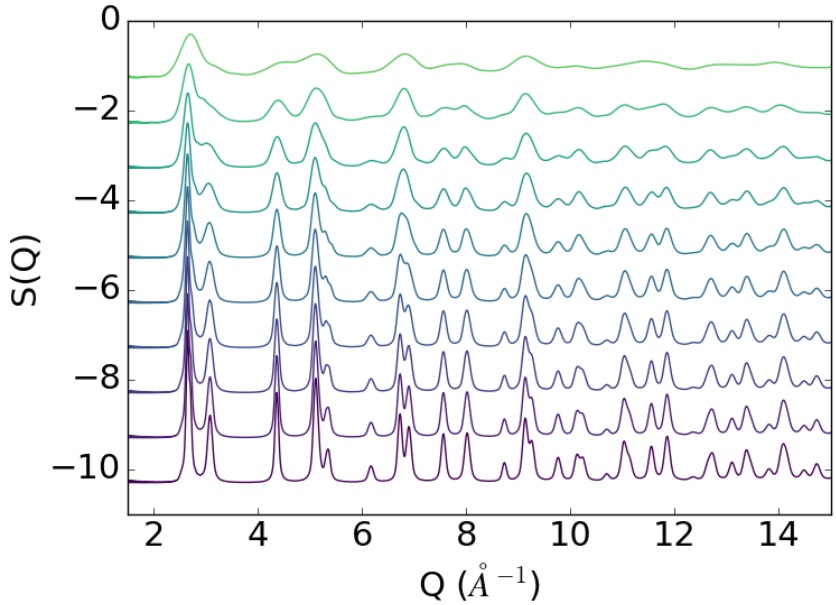

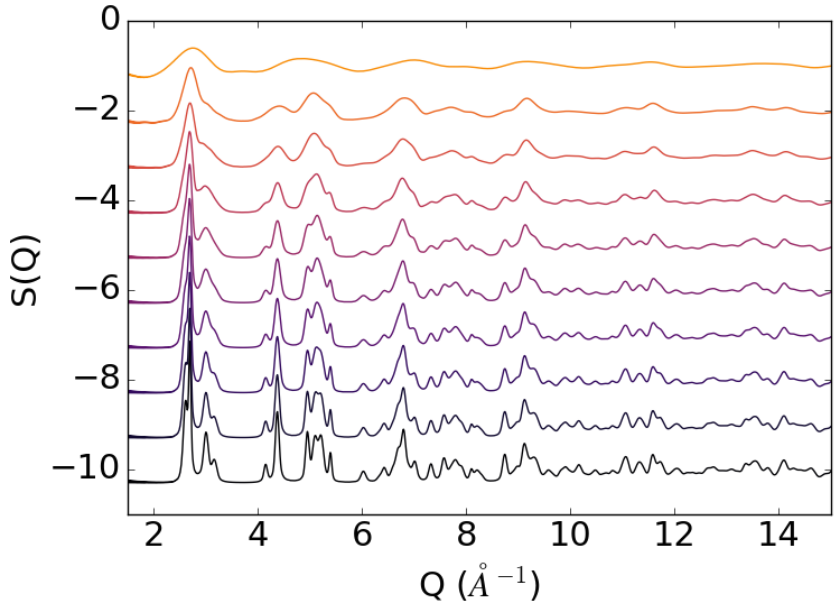

Simulated diffraction data from (top) FCC gap type models and (bottom) BCO type models of increasing size. In both series the smallest models (top) contained 115 atoms and had a longest dimension of ~2 nm and the largest models (bottom) contained ~53,300 atoms and had a longest dimension of ~18 nm. Diffraction data from the smallest nanoparticles have few distinguishing features model to model. However, the models can be readily distinguished above ~15 nm in size.

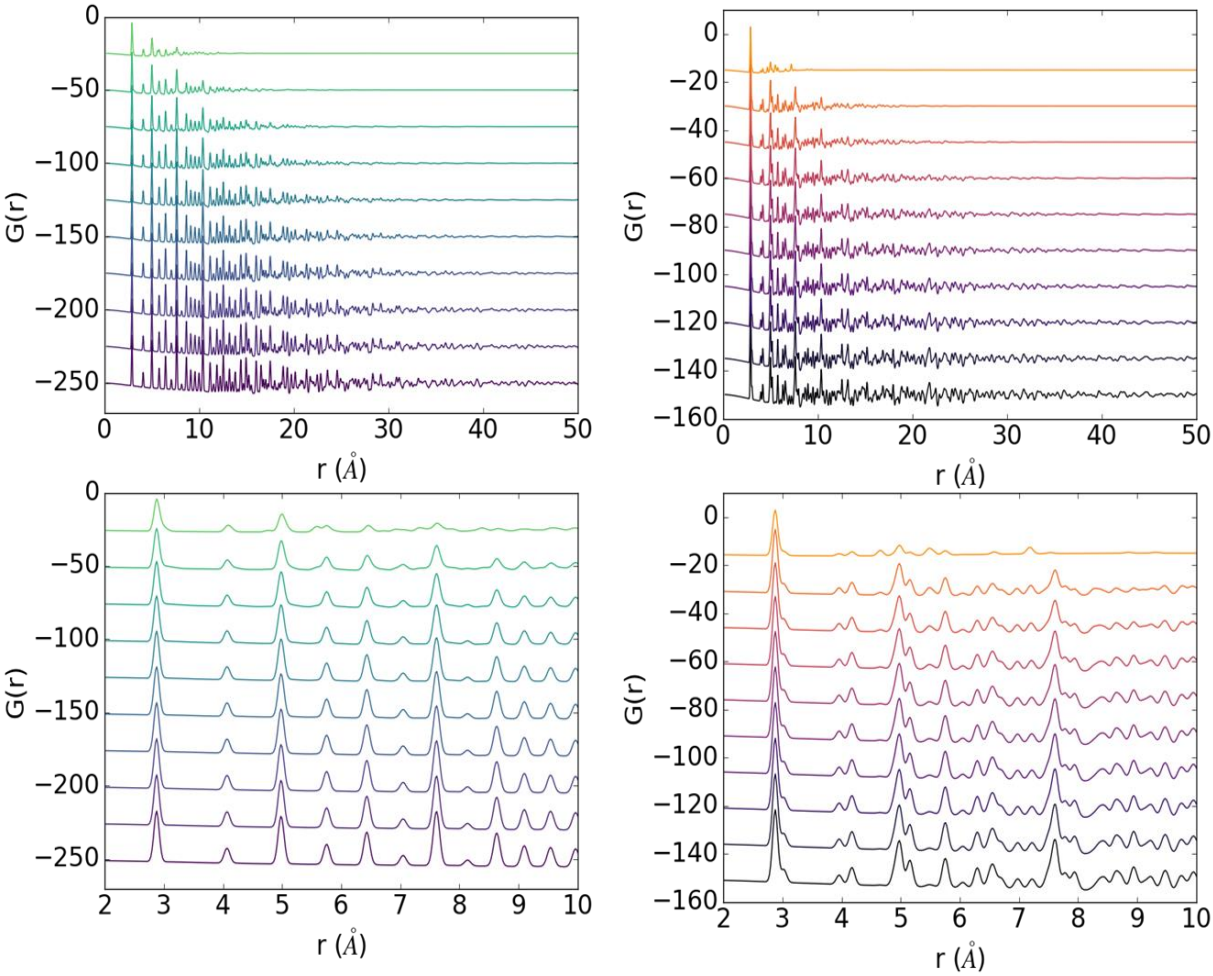

Simulated PDF data from (left) FCC gap type models and (right) BCO type models of increasing size. In both series the smallest models (top) contained 115 atoms and had a longest dimension of ~2 nm and the largest models (bottom) contained ~53,300 atoms and had a longest dimension of ~18 nm. The models can be readily distinguished at all sizes, regardless of particle size.